

A Comprehensive Astrometric Calibration of HST's WFPC2 : I. Distortion Mapping

DANA I. CASSETTI-DINESCU,¹ TERRENCE M. GIRARD,^{1,2} VERA KOZHURINA-PLATAIS,³ IMANTS PLATAIS,⁴ JAY ANDERSON,³
AND ELLIOTT P. HORCH¹

¹*Department of Physics, Southern Connecticut State University, 501 Crescent Street, New Haven, CT 06515*

²*Department of Astronomy, Yale University, Steinbach Hall, P.O. Box 208101, New Haven, CT 06520-8101*

³*Space Telescope Science Institute, Baltimore, MD 21218*

⁴*Department of Physics and Astronomy, The Johns Hopkins University, Baltimore, MD 21218*

Submitted to PASP

ABSTRACT

Wide field planetary camera 2 (WFPC2) exposures are already some 20 years older than *Gaia* epoch observations, or future JWST observations. As such, they offer an unprecedented time baseline for high-precision proper-motion studies, provided the full astrometric potential of these exposures is reached. We have started such a project with the work presented here being its first step. We explore geometric distortions beyond the well-known ones published in the early 2000s. This task is accomplished by using the entire database of WFPC2 exposures in filters F555W, F606W and F814W and three standard astrometric catalogs: *Gaia* EDR3, 47 Tuc and ω Cen. The latter two were constructed using *HST* observations made with cameras other than WFPC2. We explore a suite of centering algorithms, and various distortion maps in order to understand and quantify their performance.

We find no high-frequency systematics beyond the 34th-row correction, down to a resolution of 10 pixels. Low-frequency systematics starting at a resolution of 50-pixels are present at a level of 30-50 millipix (1.4-2.3 mas) for the PC and 20-30 millipix (2-3 mas) for the WF chips. We characterize these low-frequency systematics by providing correction maps and updated cubic-distortion coefficients for each filter.

Keywords: Astrometry: space astrometry — Stellar kinematics: proper motions

1. INTRODUCTION

We live in an era where precision astrometry is revolutionizing our understanding of the local universe. Much of this recent leap forward is due to two space-based platforms, *Gaia* and the Hubble Space Telescope (*HST*). While *Gaia* was designed from the start as an astrometric mission, *HST* had a broader scope, with its imaging capabilities, in particular, playing a major role in numerous scientific discoveries. After a meticulous calibration effort geared toward astrometry, *HST* has also proved to be a high-precision astrometric instrument, poised to compete with and complement *Gaia*. For instance, *HST* has provided accurate measurements of distant Milky-Way satellites and globular clusters (e.g., [Sohn et al.](#)

[2017](#), [2018](#); [Kallivayalil et al. 2013](#)), internal motion and rotation in globular clusters (e.g., [Watkins et al. 2015](#); [Bellini et al. 2017](#)), as well as parallaxes of various objects of interest (see review by [Benedict 2017](#); [Riess et al. 2016](#)).

HST has three advantages over *Gaia*: better resolution in crowded stellar fields, depth, and a longer time baseline for motion studies. *Gaia*, of course has the advantage of full-sky coverage and unprecedented astrometric precision at magnitudes that overlap well with a large portion of *HST* exposures. A comparison of *Gaia* DR2 ([Gaia Collaboration et al. 2018a](#)) proper-motion measurements of distant Milky-Way satellites with measurements made by various groups using *HST* data is presented in [Gaia Collaboration et al. \(2018b\)](#). Figure 15 of [Gaia Collaboration et al. \(2018b\)](#) makes it abundantly clear that the best agreement between the two platforms is obtained when *HST* measurements 1) have long time baselines (~ 10 years) and 2) are

made with thoroughly-calibrated instruments such as the ACS/WFC and the WFC3/UVIS.

Here, we will combine the attributes of *HST* and *Gaia* in order to better calibrate, astrometrically, older *HST* observations and thus make these available for a variety of proper-motion studies. Specifically, we calibrate the Wide Field Planetary Camera 2 (WFPC2), making use of all appropriate observations taken since it was installed (1993) up to its decommissioning (2009). The Mikulski Archive for Space Telescopes (MAST) includes WFPC2 observations of ~ 100 Milky-Way globular clusters and many regions of interest in the Magellanic Clouds and in the Galactic bulge, to name a few, thus offering a rich database of early-epoch astrometry for proper-motions studies. Furthermore, early-epoch, accurately calibrated WFPC2 positions can be combined not only with existing modern *HST* observations, but with new observations taken from the ground with various high-resolution imaging techniques, (e.g., the Gemini multiconjugate adaptive optics system, [Massari et al. 2016](#); [Patti & Fiorentino 2019](#)) as well as upcoming observations with *JWST*.

2. DATA SETS

The calibration scheme we develop heavily depends on the number of accumulated astrometric solutions and thus implicitly, observations. Therefore, we will use observations taken in filters F555W, F606W and F814W that have the largest archived datasets. An inventory of the exposures is presented in Table 1. We have used the MAST to obtain the corresponding processed fits files. These data were kindly shipped to us on a hard drive upon special request to MAST personnel. Comparing the MAST list of WFPC2 observations and the archived files, we find that a handful of exposures are missing from the archives: three in F555W and one in F814W.

We also choose not to use any binned exposures, thus eliminating 9 more exposures in F555W and 18 in F814W. The total number of exposures listed in column 2 of Tab. 1 thus represents the number of usable exposures that were considered in this study; the following columns indicate the number of exposures per each WFPC2 chip. The distribution of the observations in Galactic coordinates is shown in Figure 1 for each filter. Distributions are highly correlated, especially in filters F555W and F814W, indicating the photometric scientific purposes of the vast majority of these observations.

3. AIMS AND OVERALL STRATEGY

The primary purpose of this study is to identify sources of systematic errors in WFPC2 astrometry and

Table 1. List of WFPC2 Exposures

Filter	Total	PC	WF2	WF3	WF4
F555W	14828	14312	12914	13008	13031
F606W	28257	28191	28186	28249	28185
F814W	26466	26309	25507	25555	25499

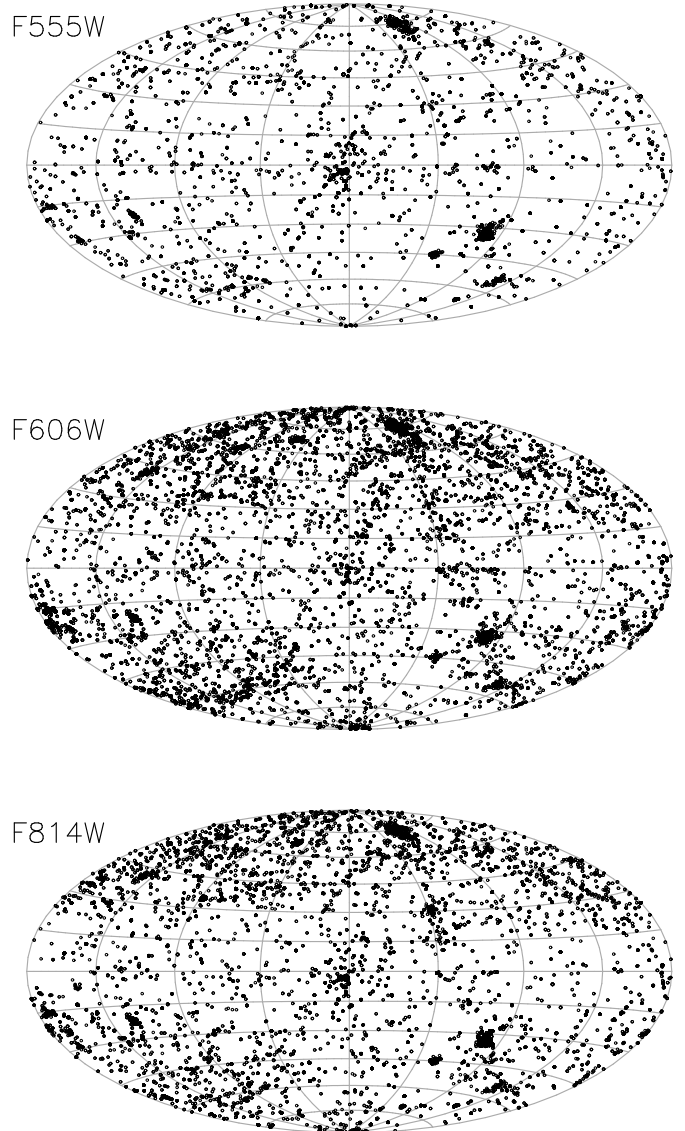


Figure 1. Galactic-coordinates distribution of observations in each filter. For reference, LMC-related observations cluster around $b = -33^\circ$, and SMC-related ones around $b = -45^\circ$.

model them as best possible. To this end, we are not particularly concerned with detection completeness and/or photometric accuracy. Achieving these requires a specific treatment for each set of observations and this was likely done when the original scientific analysis of a given data set was performed. We focus on building a stan-

standardized astrometric procedure that works reasonably well in most circumstances: crowded versus sparse fields, shallow versus deep exposures, etc. Naturally, sets of exposures that lack sufficient stars to perform transformations, one into another or into a standard catalog such as *Gaia*, will be of no use to our purpose. Such exposures include high Galactic latitude regions, very shallow exposures, and exposures focused on bright, extended objects such as solar-system planets and such.

Systematic, geometric errors are determined by stacking residuals from multiple “plate” solutions, i.e., transformations between detector pixel coordinates and standard-catalog celestial coordinates. The celestial coordinates are first transformed into standard coordinates, (ξ, η) , via gnomonic projection about a suitable tangent point for each exposure, and then rotated to align with the (x, y) pixel system of each chip based on the WCS information of the WFPC2 fits files. Thus, residuals from the transformations will be in the detector coordinate system. We adopt a general cubic polynomial transformation between rotated standard coordinates and detector positions:

$$\xi_r = a_0 + a_1x + a_2y + a_3x^2 + a_4xy + a_5y^2 + a_6x^3 + a_7x^2y + a_8xy^2 + a_9y^3 \quad (1a)$$

$$\eta_r = b_0 + b_1y + b_2x + b_3y^2 + b_4yx + b_5x^2 + b_6y^3 + b_7y^2x + b_8yx^2 + b_9x^3 \quad (1b)$$

where ξ_r, η_r are the rotated standard coordinates of a reference star and x, y are the star’s position in the detector relative to a fiducial position, in pixels, taken to be (425, 425). The twenty coefficients, a_n and b_n , are determined by an iterative least-squares procedure with outlier culling. Residuals are the differences between the standard catalog positions and calculated positions for all reference stars.

We investigate and model systematic errors, grouped by amplitude and by scale length over which they operate. For instance, the well-documented known systematics of WFPC2 are the 34th-row correction (Anderson and King 1999, hereafter AK99), and the geometric optical distortion (Anderson and King 2003, hereafter AK03). The former operates with an amplitude of 15 millipix (mpix, thereafter) over some 34 pixels of the detector and is due to a manufacturing defect in all four chips; one of every 34 rows is narrower than the rest. The latter operates with an amplitude of ~ 4 pixels over some 400 pixels (i.e., from center to edge of a chip). Systematics that operate on scales smaller than or comparable to the 34th-row correction we will call high-frequency, while those larger than the 34th

row, we will refer to as low-frequency. Our primary goal is to explore whether (geometric) systematics of high and low frequency exist beyond what was found by AK99 and AK03. We will also explore the variation of these systematics with time. The charge transfer efficiency (CTE) (Dolphin 2009) effect on positions will be explored in a following study.

Each WFPC2 chip is modeled separately as an individual unit. We use internal calibrations, meaning relative coordinate transformations between overlapping sets of exposures, as well as external calibrations, meaning coordinate transformations between WFPC2 exposures and a standard catalog. We make use of three external standard catalogs: *Gaia* EDR3 (*Gaia* Collaboration et al. 2020), one near 47 Tuc and based on ACS/WFC observations in an off-center field of the cluster (Kozhurina-Platais et al. 2015, 2018), later placed on the *Gaia* DR2 system (*Gaia* Collaboration et al. 2018a), and a third catalog of ω Cen based on WFC3/UVIS observations in the center of the cluster (Kozhurina-Platais et al. 2015). Details are provided in the following section on standard catalogs.

In the case of internal calibrations, the standard coordinates on the left-hand side of Equations 1a and 1b are replaced by the (x, y) detector coordinates from a chosen reference frame, be it a single exposure or the average of multiple exposures transformed onto a common reference system. Throughout, we shall specify whether residuals are derived from external or internal calibrations. In general, internal calibrations are used for tests of precision and consistency checks while our final distortion coefficients and maps are based solely on calibrations with external catalogs.

With the exception of some specific tests, all WFPC2 coordinates are first pre-corrected for the two known systematics: the 34th-row (AK99) and the nominal 3rd order optical distortion (AK03, also WFPC2 instrument handbook v10.0). The AK03 distortion correction makes use of a single set of cubic coefficients for all three filters, namely those in Table 5.6 of the WFPC2 instrument handbook. We will call this the *nominal* distortion. Distortion for filters F814W and F300W was explored by Kozhurina-Platais et al. (2003) as a difference between the nominal distortion and the residuals provided by the new filters, much in the same way as we do here, but using far fewer data sets and no standard external catalog.

Here we determine distortion maps as post corrections to the nominal distortion of AK03, for each filter and two epoch ranges, using the three external standard catalogs mentioned above.

4. STANDARD CATALOGS

Basic properties of the external standard catalogs are listed in Table 2. Our procedures were originally developed using *Gaia* DR2. With the recent release of *Gaia* EDR3 (*Gaia* Collaboration et al. 2020), we were able to reprocess the entire data set quickly and our results presented here are based on EDR3, although, occasionally we may refer to DR2 for some tests. From *Gaia* EDR3 we make use of all stars that have a proper-motion measurement. Since each WFPC2 chip encompasses a rather small sky area, we need every single *Gaia* star that has a reasonably well-determined position, translatable to the epoch of the WFPC2 observation. The errors in the astrometric transformations of WFPC2 star positions into *Gaia* are dominated by the *Gaia* EDR3 proper-motion errors which propagate into positional errors when backdated to the epoch of the WFPC2 observations. Accumulating residuals from such transformations over many pointings on the sky (see Fig. 1) ensures that any spatially-dependent systematics in *Gaia* (e.g. *Gaia* Collaboration et al. 2020) — much smaller in EDR3 than in DR2 — will not impact our results. Instead it is the random *Gaia* position errors at the WFPC2 observation epoch that dominate the error budget. For instance, *Gaia* stars participating in WFPC2 solutions are typically faint, peaking at $G \sim 19$, and thus have an approximate proper-motion error of $\sim 0.3 \text{ mas yr}^{-1}$. Propagating back twenty years (for early WFPC2 observations), this corresponds to 6-mas positional error, or 130 mpix for the PC and 60 mpix for the WF chips. Star-image centering errors are typically below these values for the WFPC2. Nevertheless, averaging hundreds of thousands of such residuals allows us to characterize systematic WFPC2 distortion beyond that of the applied, nominal distortion correction.

The 47 Tuc catalog is the most precise and accurate among the three standard catalogs. It is based on ACS/WFC F606W observations (Kozhurina-Platais et al. 2015) of an off-center field of the cluster. The off-center pointing allows good overlap with *Gaia* measurements, despite its crowdedness limitations. The original 47 Tuc catalog was improved using *Gaia* DR1 (*Gaia* Collaboration et al. 2016) by Kozhurina-Platais et al. (2018). Kozhurina-Platais (private communication) used *Gaia* DR2 to further improve the positions; it is this version of the catalog with which we started to work. Upon inspection of a transformation of the catalog positions into *Gaia* DR2 positions, we noticed that, bright, well-measured stars in *Gaia* still presented significant 3-rd order terms. Therefore, we have used *Gaia* DR2 well-measured, bright stars to adjust for

residual distortion in the positions of the catalog. We have also used well-measured stars (~ 5500 stars with $G \leq 20$) to place the relative proper motions of the catalog onto the absolute system of *Gaia* DR2. Finally, for convenience in our exploration of systematics within magnitude ranges, we have adjusted the catalog’s F606W instrumental magnitudes to the *Gaia* G magnitude system. This was done by adding a constant to the 47 Tuc instrumental magnitudes. A plot of magnitude differences as a function of *Gaia* ($G_B - G_R$) color showed no trends. The rms of the differences was 0.03 mag. Proper-motion uncertainties in the 47 Tuc standard catalog have an upper limit of 0.50 mas yr^{-1} , with an average of 0.12 mas yr^{-1} .

The ω Cen catalog (Kozhurina-Platais et al. 2015) is based on WF3/UVIS F606W observations in the center of the cluster. As such, a *Gaia*-based astrometric adjustment is not possible, as there are very few *Gaia* stars in this very crowded region, and those present are rather poorly measured (see also Kozhurina-Platais et al. 2018). From this original catalog, we keep objects having at least 5 observations and with proper-motion uncertainties $\leq 10.0 \text{ mas yr}^{-1}$. To place the instrumental magnitudes on a standard system we do a match with *Gaia* DR2. Of the 263 matches, we use 90 suitable stars (neither too faint nor too bright) to determine the magnitude offset (with an rms of 0.03 mag). After applying the offset, we find that the faint limit of the catalog is close to the overall *Gaia* limit (see Tab. 2). Proper motions are relative, however this will not affect our solutions, since the vast majority of stars that will be used in WFPC2 transformations are cluster stars (and thus share a common systemic motion). Mean proper-motion uncertainties are ~ 0.14 to 0.20 mas yr^{-1} for stars with $G > 16$. Brighter stars, $G \sim 14 - 16$, have larger proper-motion uncertainties, with a mean of ~ 1.0 to 2.0 mas yr^{-1} . The largest uncertainties are in μ_δ , in both magnitude ranges.

The advantage of the two cluster-based standard catalogs is that they are at epochs closer to the WFPC2 observations than is *Gaia* EDR3; the 47-Tuc catalog is substantially deeper and the most precise. These cluster-based standard catalogs will serve as useful checks on the *Gaia* EDR3 results. In Tab. 2 we also list the range of the number of WFPC2 exposures used to perform suitable solutions into these catalogs, as well as the range of the number of reference stars per chip used in such solutions. The ranges reflect variations between filters and chips (see also Section 7.2).

Table 2. Standard Catalogs Properties

Catalog	Instr.	System	$\langle Epoch \rangle$	G -limit	# WFPC2 exposures	# ref stars/chip
<i>Gaia</i> EDR3	<i>Gaia</i>	absolute	2016.0	~ 21.0	2600 - 5200	20 - 600
47 Tuc - off cen.	ACS	absolute	2007.8	~ 25.3	32 - 132	50 - 1600
ω Cen - center	WF3	relative	2011.2	~ 21.2	18 - 26	400 - 4700

5. CENTERING ALGORITHMS

In this section various centering algorithms are considered and their performance on WFPC2 stellar images evaluated. We feel it is important to convey what we have learned in this regard, although admittedly the details may not be of interest to all readers. For this reason we state that the two centering methods adopted for determining our final distortion maps and corrections to the cubic-distortion terms are 2-D Gaussian centering and the effective PSF (ePSF) algorithm, as detailed below. Discussion of the derivation of distortion corrections resumes with Section 7.

The best choice of algorithm for centering WFPC2 stellar images is not obvious, given our intended purpose. Our goal is to minimize the noise in the average residuals generated by transformations into the standard catalogs. When using *Gaia* EDR3 as the standard catalog, propagation of the EDR3 proper-motion errors to the WFPC2 epoch will be the dominant source of scatter in the residuals, provided the WFPC2 centers are even moderately well-determined. In which case it is important to choose a centering algorithm that performs over a wide range in magnitude (even into the realm of saturated images) in order to maximize the number of *Gaia* stars that can be utilized as reference stars. Conversely, when employing the 47 Tuc and ω Cen standard catalogs, centering precision of the WFPC2 stellar images is paramount, given the higher precision of these external catalogs and the relatively few WFPC2 exposures available in these areas. Finally, there is the practical matter of computational speed to consider.

In general, the process of determining precise centers of stellar images consists of three steps: pre-processing the image data to properly calibrate for detector response, detecting stellar sources as groups of pixels with signal above the background noise, and then refining the positions of each source by fitting the nearby pixels with some model function. The MAST provides calibrated `_c0m.fits` files for every WFPC2 exposure, i.e., images that are bias-subtracted, dark-subtracted, and flat-fielded. Together with each target image, a bad-pixel mask is also provided (`_c0m.fits` files). We split these multi-extension FITS files and treat each chip as a separate entity.

For most of the centering methods that we explore the source-detection step is performed using the code

Source Extractor (SExtractor, version 2.19.5) developed by Bertin & Arnouts (1996, 2010). Based on an image and its corresponding bad-pixel mask, SExtractor detects objects and provides preliminary centers, instrumental magnitudes, and other image parameters. For WFPC2 images, regions along two edges of each chip are spoiled by vignetting from the four-faceted pyramid mirror and these are among the marked pixels in the bad-pixel masks. Similar limits are also given in the WFPC2 instrument handbook. However, we found the astrometry degrades over a somewhat wider region along these edges than is suggested by the masks and the WFPC2 handbook and, thus, we adopt a more restricted usable area. Specifically, for all chips we only accept sources located between 75 and 795 pixels, in both axes. After preliminary tests using a range of SExtractor parameter values, we decided on a small size for the local background (`BACK_SIZE = 16` pixels) in order to detect as many objects as possible in crowded areas with elevated backgrounds, such as cluster cores. The input FWHM parameter chosen varies by chip and filter. For the PC we have used 1.6, 1.6, 1.8 pix for filters F555W, F606W and F814W, respectively. For the WF we have used 1.2, 1.3, 1.4 pix for filters F555W, F606W and F814W, respectively. These values were determined from the peaks of the distributions of the FWHM for each chip and filter.

A number of image fitting methods were explored; each is described in the following subsections.

5.1. 2D Gaussian Centering

Two-dimensional, elliptical Gaussian functions (2DG) are fit to the intensity profile of each object. We use the Yale centering routines upgraded for CCD data from the original code (Lee & van Altena 1983), with centers from SExtractor serving as initial values for the non-linear fitting algorithm. Compared to the other methods tested, this algorithm is fast, and performs well for bright, partially saturated stars, enabling the largest overlap with *Gaia* EDR3 stars. We note that the analytical form of this fitting function allows it to vary its width and shape across the chip.

5.2. ePSF Centering

The ePSF code described in Anderson and King (2000) utilizes an *effective* PSF built empirically from

observations and has become somewhat of an *HST* standard. This code (hst1pass.2019.10.11) includes its own detection algorithm and also provides object centers, instrumental magnitudes and a quality-of-fit parameter (q). The mode in which we run the program employs an existing library of ePSFs specifically constructed for the WFPC2; these were provided along with the software. For each chip, a 3×3 x-y grid of ePSFs is contained in the library. WFPC2 ePSF libraries exist for only two of our filters: F555W and F814W. Thus, for F606W, we have used the F555W library ePSFs. As with the other centering methods, only sources in the area between 75 and 795 pixels, in both axes, are accepted.

The ePSF algorithm is fast and provides the best object centers for the WF as we will further detail. Because the ePSF algorithm fits only the inner 5×5 pixels of an object, the code tends to discard a large number of bright stars that are nearing saturation but are otherwise measurable, astrometrically. Where the code really shines is in providing very high precision centers for fainter stars. As a consequence, there will be a limited magnitude-range overlap with *Gaia* EDR3 stars, and this overlap is where errors in *Gaia* EDR3 increase rapidly. For reference, we use only objects with q between 0.0001 and 1.0.

5.3. *Dolphot Tiny Tim PSF Centering*

The DOLPHOT package (Dolphin 2000) version 2.0 was used to test the astrometric performance of image centers determined with Tiny Tim PSFs. These are optical-model PSFs based on the *HST* TinyTim simulator (Krist et al 2011) for each camera, chip and filter. Pre-processing included masking bad pixels, separating into the four chips and calculating the sky background, all done following the Dolphot manual recommendations. Consistent with previous schemes, we use only images detected within 75 and 795 pixels (both coordinates) of each chip. The algorithm is geared toward optimizing source detection and photometry but is prohibitively slow for our intended application.

5.4. *PSFEx*

PSFEx (PSF Extractor) is a code developed by Bertin & Arnouts (2010) that constructs empirical models of a spatially varying PSF from images pre-processed with SExtractor. We tested version 3.17.1 of this code. To build the PSF library, we use the 47-Tuc core F555W data set of 636 160-sec exposures that were offset by no more than 1 WF pixel (PI Gilliland, PID 8267) taken in July 1999. Objects detected with SExtractor are candidates for PSF computation: we further limit these to a FWHM range between 0.8 and 3.0 pixels, a minimum SNR = 50 and a maximum ellipticity of

0.2. Each object thus selected, is cut out from the image with a square raster size of 5×5 pixels (the “vignetting” parameter in PSFEx) and then fed into the PSF-model builder. Our selection yielded $\sim 162,000$ PSF stars for the PC, and $\sim 223,000$ PSF stars for the WF chip. The PSF stars are well-distributed over the chip area. To account for spatial variation, we use a 5×5 $x - y$ grid of PSF models across each chip and linear interpolation. Each PSF is built in super-resolution mode, utilizing a PSF size of 7×7 pixels. The parameter controlling the under/oversampling of the PSF is known as “sample” in the PSFEx code; we explored a range of values between 0.8 and 3.0 with a step of 0.2.

Once the PSF model is built, SExtractor is run again to obtain new centers based on PSF-fitting for all detections in our target exposure, which was a 1400-sec F555W exposure of 47 Tuc (PID 6114, epoch 1995.815) that overlaps with the 47 Tuc standard catalog. Astrometric solutions into this catalog, including up to third-order polynomial terms, were performed. The best solutions obtained were for PSFs using a sampling factor of 1.2 for the PC and 2.0 for the WF. That is, these values resulted in the smallest standard errors of the transformation while retaining a reasonable number of stars in the solution. The centers were found to have a small pixel-phase bias (see below, in Section 6.2). The algorithm is relatively cpu-intensive, which prevented our exploration of any possible variation of the PSF library with epoch of observation. This latter aspect also affects the ePSF algorithm which has a library based on a single-epoch data set.

5.5. *Fourier technique + 2D Gaussian*

This procedure is somewhat different in that it applies additional pre-processing before the image detection and fitting steps. It begins by creating an idealized diffraction-limited image of a point source using the known pixel scale, the parameters of the primary aperture with central obscuration of the secondary mirror, and the wavelength of observation. The resulting image is then used to deconvolve the WFPC2 exposure in the Fourier domain, resulting in a true estimate of the Fourier transform of the image. However, at higher spatial frequencies, the noise in the Fourier domain begins to dominate, and therefore a low-pass filter is applied. This filter is a Gaussian filter where the wings have been suppressed by multiplying by a Butterworth filter and thresholding. This effectively sets extremely low but non-zero values to zero. After application of the filter, the resulting frame is then inverse-transformed to arrive at a Fourier-reconstructed image. Finally, this reconstructed image is processed as in Sec. 5.1. The

Fourier technique has the advantage of suppressing the pixel-phase bias. However, faint objects are lost in the Fourier reconstruction (see Secs. 6.2, 6.1).

6. COMPARATIVE ASSESSMENT OF THE CENTERING ALGORITHMS

To illustrate the head-to-head centering performance of the various algorithms we select an appropriate WFPC2 exposure within the area of the 47 Tuc standard catalog, which is the deepest and most precise of the standard catalogs (Sec. 4). We choose an F555W 1400-sec exposure taken at epoch 1995.815 (PID 6114), this wavelength passband being the most undersampled of the three filters considered, i.e., the most demanding scenario. Two aspects of the various centers are examined: the astrometric precision as measured by a transformation into the 47 Tuc standard catalog positions, and a diagnosis of the centering algorithm’s pixel-phase bias.

Note that the test results from the transformation into an external standard catalog, while providing uniformity in the comparison, will include errors of this external catalog. These errors are largely the proper-motion errors of the external standard catalog propagated into positions at the epoch of the WFPC2 exposure. In a future study, we will present a more in-depth analysis of the centering precision as also determined from relative astrometry, i.e., from repeated, offset WFPC2 exposures.

6.1. Astrometry from Transformation into a Standard Catalog

Each set of centers for this test exposure are transformed into the epoch-adjusted, gnomonic projected and rotated celestial coordinates of the 47 Tuc standard catalog using Eq. 1 and the procedure described in Sec. 3. We note that while 2DG, ePSF and Fourier positions were pre-corrected with the 34th-row correction and the nominal distortion, the Dolphot/TinyTim and PSFEx positions were not. This does not affect the conclusions of this particular test since third-order terms are included in the transformations, thus absorbing residual distortion, while the 34-row issue will make a negligible contribution to the overall scatter of the residuals, its amplitude being at most 15 mpix and only affecting a very small subset of images, those that happen to fall on such rows. The residuals of the resulting transformations will be the quadrature sum of the centering errors of each algorithm on an WFPC2 exposure and the position errors of the external standard catalog. The latter are dominated by the proper-motion errors of the 47 Tuc standard catalog propagated to the epoch of the WFPC2

observation, i.e., some 12 years. Considering an average proper-motion uncertainty of 0.12 mas/yr (Sec. 4), the position errors of the standard catalog are ~ 31 mpix for the PC and ~ 14 mpix for the WF chips.

Residuals from each centering algorithm’s transformations are plotted in Figure 2 as a function of G magnitude. We show residuals along the detector y -axis; x -residuals show very similar trends. Each centering algorithm and each chip are specified in the respective panel. We also note the total number of stars that participated in the solution, and the standard error of the solution in mpix.

As expected, the algorithms perform better with the PC than with the WF chips. This is a consequence of the undersampling; PC images are better sampled than WF images by a factor of ~ 2 . The ePSF algorithm performs best in all four chips, however, the limits imposed on the q parameter have as a consequence the discarding of objects between $G = 18 - 20$ mag. Performance of the PSFEx algorithm follows behind that of the ePSF algorithm. Although the standard deviation of the PSFEx residuals appears much larger than that of the ePSF residuals (as seen in Fig. 2), this is in part due to the larger magnitude range covered by the PSFEx algorithm. For stars in common between the two, the PSFEx residuals have scatter that is from 10% to 70% larger, depending on the chip. At the bright end, PSFEx effectively outperforms the ePSF algorithm by retaining many well-measured stars, while at the faint end it outperforms the 2DG algorithm in precision.

The TinyTim+Dolphot algorithm appears to be the most affected by undersampling. For the WF, the residuals are very scattered, and show a bimodal distribution, which is quite prominent at $G \leq 22$. This bimodal distribution is a result of large pixel-phase bias (see Sec. 6.2).

The Fourier technique, while displaying a scatter comparable to that of the 2DG algorithm, loses stars at the faint end. Also, chip WF2 performs more poorly than WF3 and WF4 due to the density of stars in WF2, which is closest to the cluster center. It is interesting that it recovers well the astrometry of bright stars almost into the saturation regime.

6.2. Pixel-phase Bias

Pixel-phase bias is measured by constructing “bias curves,” one in each coordinate, for a given set of image centers given in pixels. To do so, the stars’ positions are ordered by fractional pixel phase, from 0 up to but not including 1. Once ordered, each star’s pixel phase is compared to that at the same rank for a set containing an equal number of stars but having a *uniform* pixel-

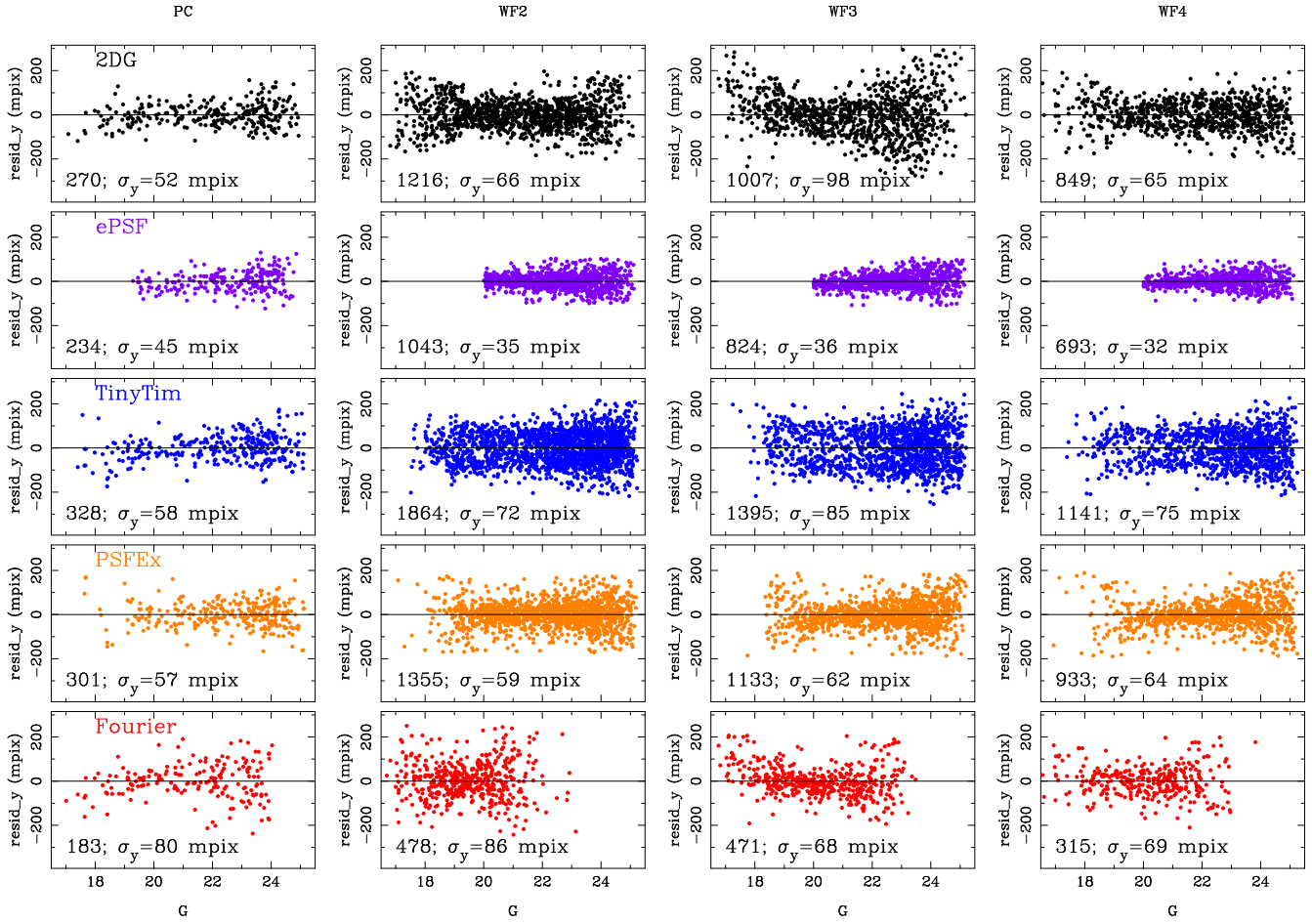


Figure 2. Residuals from the transformation of star centers from an F555W, 1400-sec exposure (PID 6114) into the 47 Tuc standard catalog as a function of G magnitude. Each panel represents a centering algorithm and chip as specified. The number of stars participating in the solution and the standard error of the solution are also indicated for each case. The contribution of the external catalog position errors to the error budget is ~ 31 mpix for the PC and 14 mpix for the WF.

phase distribution. The differences between measured pixel phase and that expected for a uniform distribution, as a function of pixel phase itself, is a representation of the pixel-phase bias curve.

For a set of centers with random (unbiased) pixel phases, such curves will be flat, with a level of noise that depends on the number of stars in the sample. The curves of pixel-phase biased samples will exhibit structure that is often, but not always, roughly sinusoidal.

In Figure 3 we plot pixel-phase bias curves for the five centering algorithms explored here and for each chip. We use the coordinates as they are output from the centering algorithm, i.e., with no distortion pre-correction as this will alter the pixel-phases. Only stars that participated in the solution into the standard catalog (see Sec. 6.1) are included in these plots. For all algorithms the PC-curves are noisy and thus it is unclear which algorithm is best, if any. For the WF, the TinyTim algorithm has the strongest pixel-phase bias followed by the 2DG. The ePSF, PSFEx and Fourier algorithms have relatively flat curves. While more exploration is needed especially for the PC, we have established that for high-precision, relative astrometry, the TinyTim and 2DG algorithms are not as desirable, while the ePSF, PSFEx and Fourier are promising. The ePSF however, discards the bright end, while the Fourier algorithm loses the faint end.

This, along with the relative sizes of the transformation standard errors previously discussed, lead us to adopt the ePSF centers when maximum precision is desired, and the 2DG centers when bright-star coverage is important.

7. DISTORTION MAPS

7.1. Exploring high frequency systematics

In Sec. 3 we defined high-frequency systematics as those manifested over scales of the order or 34 pixels or less. The pixel-phase bias does qualify for this type of systematic. We gave a brief introduction and demonstration of this bias in Sec. 6.2. A full exploration of its effect on high-precision relative astrometry is beyond the scope of this paper and will be presented elsewhere. Importantly, its contribution to the maps we build now will be random and at a level below that introduced by other sources such as proper-motion errors from the standard catalogs.

In order to explore scales below 34 pixels, but larger than one pixel, we need a residual map with a high resolution, ideally of the order of a few pixels. In each such resolution element (or cell) we need a sufficient number of residuals to overcome the random errors, and furthermore require a balanced distribution of residuals over

the resolution elements. In other words, if residuals are clumped spatially to thousands in some cells and none or a few in other cells, then the map will be compromised. At this resolution *Gaia* does not provide such a density and distribution of stars in the WFPC2 exposures.

Instead, we search for dithered WFPC2 exposure sets that are dense in stars and with small offsets between exposures. For instance, a 47 Tuc core set (PI Gilliland, PID 8267) of 636 160-sec exposures appears to fit the bill; however its offsets are at most 1 WF pix, meaning the stars will be clustered in certain cells of an average-residual map. Thus, to supplement this data set, we search for other appropriate exposures, specifically in cluster fields. Table 3 lists the exposure sets resulting from the search; these we use to explore high-frequency systematics. The aim of this exercise is to find presumed chip-construction-related systematics, beyond the known 34th-row issue. As such, time variations and filter differences are not relevant, allowing us to stack residuals from various exposure sets taken at different epochs and with different filters.

The process is as follows: detection and centering is done with the *HST* code using ePSFs. Pre-corrections for 34th-row and (nominal) optical distortion are applied. For each exposure set, we choose one exposure and use its set of object positions to serve as an internal reference “catalog.” The set of object positions from each of the remaining exposures in this exposure group are transformed into the reference set using third-order polynomials. Once all exposures’ object lists are on the same system — that of the reference exposure — we construct an internal catalog by averaging repeated measures of the same object, with sigma-trimming to reject outliers. Positions within a given tolerance (2 PC pix, 1 WF pix) are deemed to be of the “same” object. Each exposure’s object list is then transformed into this internal, average catalog and the residuals stored and binned into cells based on pixel coordinates within the chip. Finally, for each chip, we stack residuals from all exposure sets and filters, deriving mean residual vectors on a per-cell basis, i.e., a 2-d residual map.

Properties of the exposure sets used in our high-frequency mapping are given in Tab. 3. For reference, we give the total number of residuals per set used in the map construction along with the standard deviation of the residual distribution for chip WF2. One exception is the data set of cluster NGC 6752 which was taken only with the PC; the units for this set are in PC pixels. The largest spatial offset within an exposure set is also listed. For the 47 Tuc core set, which yields the most residuals, we use only every 10th residual available, so as not to

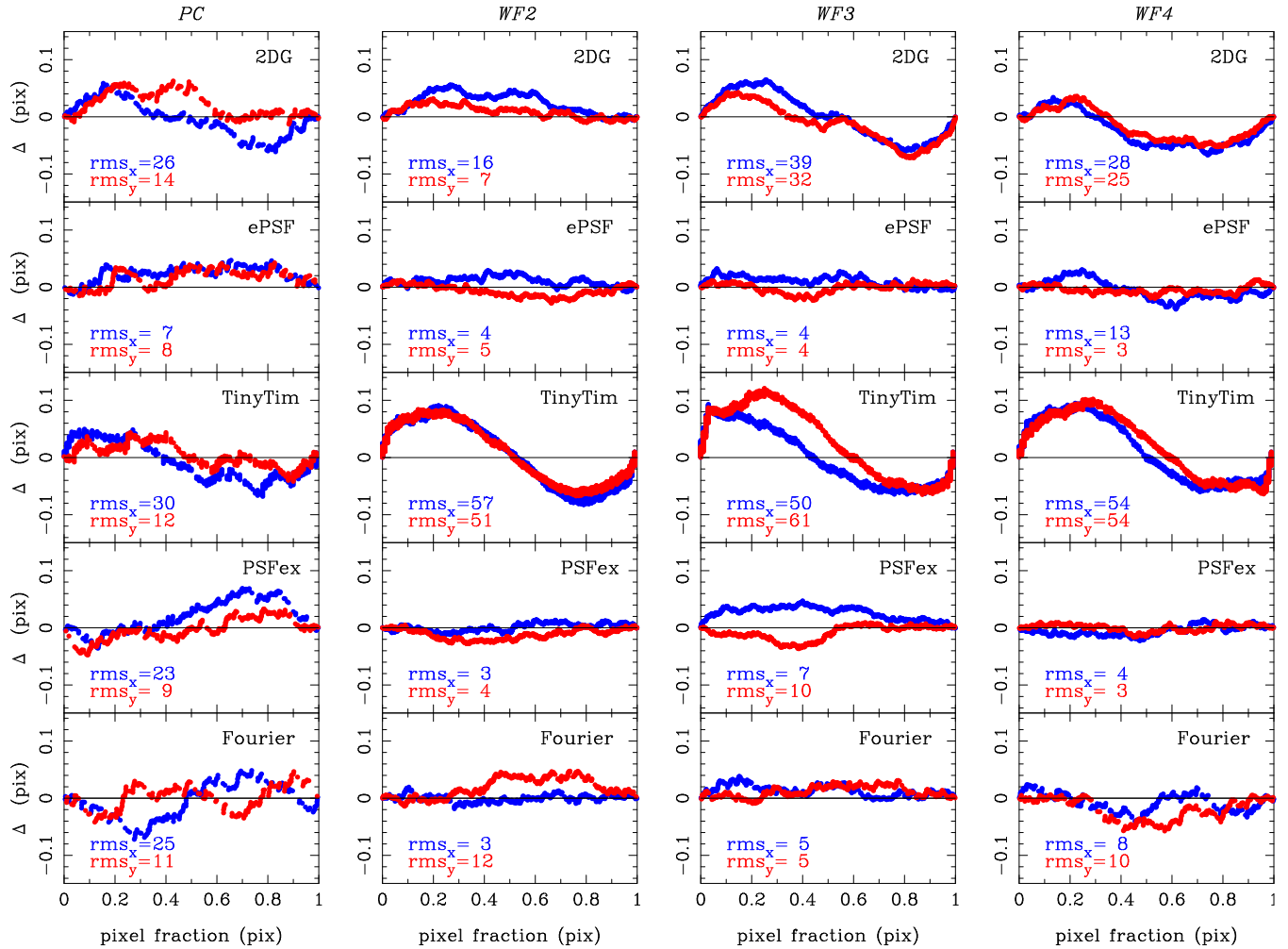


Figure 3. Representation of the pixel-phase bias associated with each centering algorithm along the x and y chip axes and for each WFPC2 chip, as labeled. Shown are differences between the measured pixel phase and that expected from a uniform distribution, as a function of pixel phase itself (see Sec. 6.2). The rms above that expected for a randomly distributed sample of the same size is also given for each axis, in mpix.

allow this set of exposures to completely dominate the map.

A map is built by specifying the cell size (i.e., resolution), a smoothing radius, and a maximum allowed residual amplitude, so as to eliminate outliers. Within each cell an average residual vector is calculated (we opt to use a sigma-trimmed mean) along with its statistical uncertainty, i.e., the standard deviation divided by the square root of the number of residuals in the cell. We discard residuals exceeding 200 mpix (in both PC and WF) to avoid undue influence by possible outliers. Two sets of maps are constructed, one with a cell dimension of 10 pixels and smoothing radius of 7 pixels, and a second set using a cell size of 6 pixels and smoothing radius 4 pixels. The 10-pixel resolution map has of the order of 560 residuals per resolution element. The formal error of the computed mean residuals is on average 1.5 mpix for the PC and 1.3 to 1.6 mpix for the WF chips. The 6-pixel resolution map has of the order of 190 residuals per resolution element. The formal error of the computed mean residuals is on average 2.7 mpix for the PC and 2.3 to 2.6 mpix for the WF chips. Figure 4 plots the mean residual vectors of the 10-pixel resolution map. Any resolution element that had an average residual $|r| > 20$ mpix for the PC and $|r| > 10$ mpix for the WF was excluded from the plot, as these were determined to be outlier values. Beyond the 34-row problem, there is no indication of any additional systematic pattern related to the chip manufacturing process, such as was found for the WF3 and ACS cameras (Kozhurina-Platais et al. 2016). Inspection of the 6-pixel resolution map, although noisier than the 10-pixel map, also reveals no discernible systematic pattern.

7.2. Exploring low frequency systematics

7.2.1. Map construction

Systematics with a spatial extent larger than 34 pixels would most likely be due to uncorrected optical distortion. Therefore, separate maps are constructed for each filter. Residual maps based on each of the three, external standard catalogs listed in Tab. 2 will be examined. The ω Cen-center catalog has overlap only with F555W exposures, while the 47 Tuc off-center and *Gaia* EDR3 catalogs have overlap with exposures in all three filters. We explore residuals generated from both 2DG and ePSF positions.

Pixel coordinates are pre-corrected for the 34th row and nominal cubic distortion. For each observation and chip, external catalog coordinates are transformed into chip coordinates and a cubic solution is performed between these and the pixel coordinates of the WFPC2

exposure. Solutions into *Gaia* EDR3 are retained only when all three of the following conditions are met: the standard error of the solution in both coordinates is less than 0.7 pix for the PC and 1.5 pix in the WF, the scale term in both coordinates deviates by less than 10% from its nominal value, and the number of reference stars in the solution is larger than 20 for the PC and larger than 30 for the WF chips. Solutions that do not meet these requirements are discarded from the analysis. A similar scheme is adopted for solutions into the other two standard catalogs, always verifying the quality of the solution.

Finally, residuals are stacked and averaged by resolution element, as before, producing a residual map. For *Gaia* EDR3 residuals, we also force each resolution element of the map to not have more than 4 residuals of the same *Gaia* star. This minimizes the contribution of any poorly-measured *Gaia* stars to the average for any given resolution element. We also restrict residuals to be only from *Gaia* stars with $G = 11 - 20$, and discard outlier residuals, i.e. with absolute values larger than 2 pix for the PC and 1 pix for the WF.

For the low-frequency maps a 50-pix resolution element is used and a smoothing radius of 50 pix. The standard error of the average is calculated for each resolution element, as the standard deviation of the residuals divided by the square root of the number in the cell. Table 4 lists the average properties of the derived maps for each catalog, filter, and centering algorithm. The median standard error, in mpix, per resolution element is also listed, as is the number of residuals per resolution element. For the standard error, we give only the x-coordinate values, with y-coordinate results having similar values. Also listed is the total number of residuals that participated in the construction of each map. The standard error per resolution element is the primary indicator of map quality. The *Gaia* EDR3 maps supersede our initial *Gaia* DR2-based maps. The DR2 maps had median errors that are a factor of 1.4 to 1.5 larger than those of the EDR3 maps, due to the DR2 catalog's less precise proper motions as well as it having a smaller number of stars available for the solutions.

Inspecting the *Gaia* EDR3 map properties in Tab. 4, one sees that maps using the 2DG centering algorithm have better standard errors than those using the ePSF algorithm; this is simply due to the substantially larger number of residuals that participated in the construction of the 2DG maps, consistently across all three filters. It is also an indication that the dominant source of error in the map is due to proper-motion errors in *Gaia* EDR3, i.e., differences in the errors associated with the centering algorithms are not discernible in this circumstance.

Table 3. List of exposure sets used for the high-resolution map

Filter	Target	N_{resid}	σ_x (WF mpix)	σ_y	N_{exp}	Offset (WF pix)	Exp. time (sec)	Epoch	PID
555	47 Tuc core ¹	170020	19	18	636	1	160	1999.5	8267
555	ngc 6341	334582	46	48	128	176	10,100,400	2008.1	11077
555	ngc 6441	154052	31	35	36	4	160	2007.3	10474
555	<i>ngc 6752</i> ²	309365	27	30	162	563	2,26,80	1994.6	5318
606	ngc 6397	68625	20	18	121	7	500,600	2005.2	10424
606	ngc 6656 group1	47494	14	14	24	16	260	1999.1	7615
606	ngc 6656 group2	57619	15	16	24	16	260	1999.1	7615
606	ngc 6656 group3	59351	17	18	24	16	260	1999.1	7615
606	ngc 7078	38422	42	44	33	9	300,500	2001.4	9244
814	47 Tuc core ¹	195072	19	16	653	1	160	1999.5	8267
814	ngc 5139	72232	28	27	21	12	80	2008.1	11030
814	ngc 6121	37048	34	39	166	23	600,700	1995.2	5461
814	ngc 6205	88870	20	18	30	26	23,140	1999.9	8278
814	ngc 6397	88922	21	19	126	24	600	2005.2	10424
814	ngc 6656 group1	162917	15	15	64	7	260	1999.1	7615
814	ngc 6656 group2	182913	20	20	64	8	260	1999.1	7615
814	ngc 6656 group3	180089	19	18	64	6	260	1999.1	7615
814	<i>ngc 6752</i> ²	281132	20	20	146	562	50,160	1994.6	5318

1 - used only every tenth residual

2 - only PC exposures; units are PC pixels

This is not the case for the special catalogs; ePSF-based maps are slightly better than 2DG ones, while the numbers of residuals in the two algorithms' maps are comparable. Thus, the precision of the proper motions of these catalogs allows for the centering precision's contribution to the total error budget to become apparent. This is particularly obvious for the 47 Tuc catalog maps, while being somewhat more ambiguous for the ω Cen catalog.

Based on the standard error estimates in Tab. 4, the overall best maps would seem to be those using *Gaia* EDR3 with 2DG centering, although the pairing of the other two standard catalogs with ePSF centering follow close behind. In fact, the latter combination appears to be the better choice for the PC in all filters. With this in mind, we will pursue to construct weighted averages of the maps derived from *Gaia* EDR3 using 2DG centering along with maps derived using the two special standard catalogs and ePSF centering.

7.2.2. Centering-Algorithm Field Effects

Before spatial maps based on different centering algorithms can be combined, it must be demonstrated that differences between the two types of centers themselves do not introduce a spatial variation. To check for this, we select roughly 10% of all WFPC2 exposures in the three filters and, for each, transform 2DG positions of anonymous stars into ePSF positions of the same stars

using general cubic terms, similar to Eq. 1 but using raw positions. Choosing the best such solutions – those with at least 200 stars in common and standard errors less than 80 mpix – residuals are accumulated per chip and filter. From these we construct low-frequency residual maps as before, but in this case the maps represent any artificial field dependence due to the differences in centering method.

These 2DG-into-ePSF maps do show significant structure, in all chips and filters. A measure of the significance of a map is its mean χ^2 ,

$$\langle \chi^2 \rangle = \sum (r/\sigma)^2 / N \quad (2)$$

where r is the signal in a map element, σ its uncertainty, and N is the total number of elements.

The 2DG-into-ePSF maps have $\langle \chi^2 \rangle$ values of ~ 3 for the PC, and range from 4 to 14 for the WF chips, the largest values being found for filter F606W. Thus, 2DG-based maps *cannot* be combined with ePSF-based maps, unless the former are somehow first put onto the “system” of the latter. Fortunately, the just-constructed 2DG-into-ePSF maps can be used to accomplish exactly this; a simple subtraction of the appropriate 2DG-into-ePSF map from any 2DG-based map will adjust it to the ePSF system of centering. Due to the large number of residuals used to build them, subtracting the 2DG-

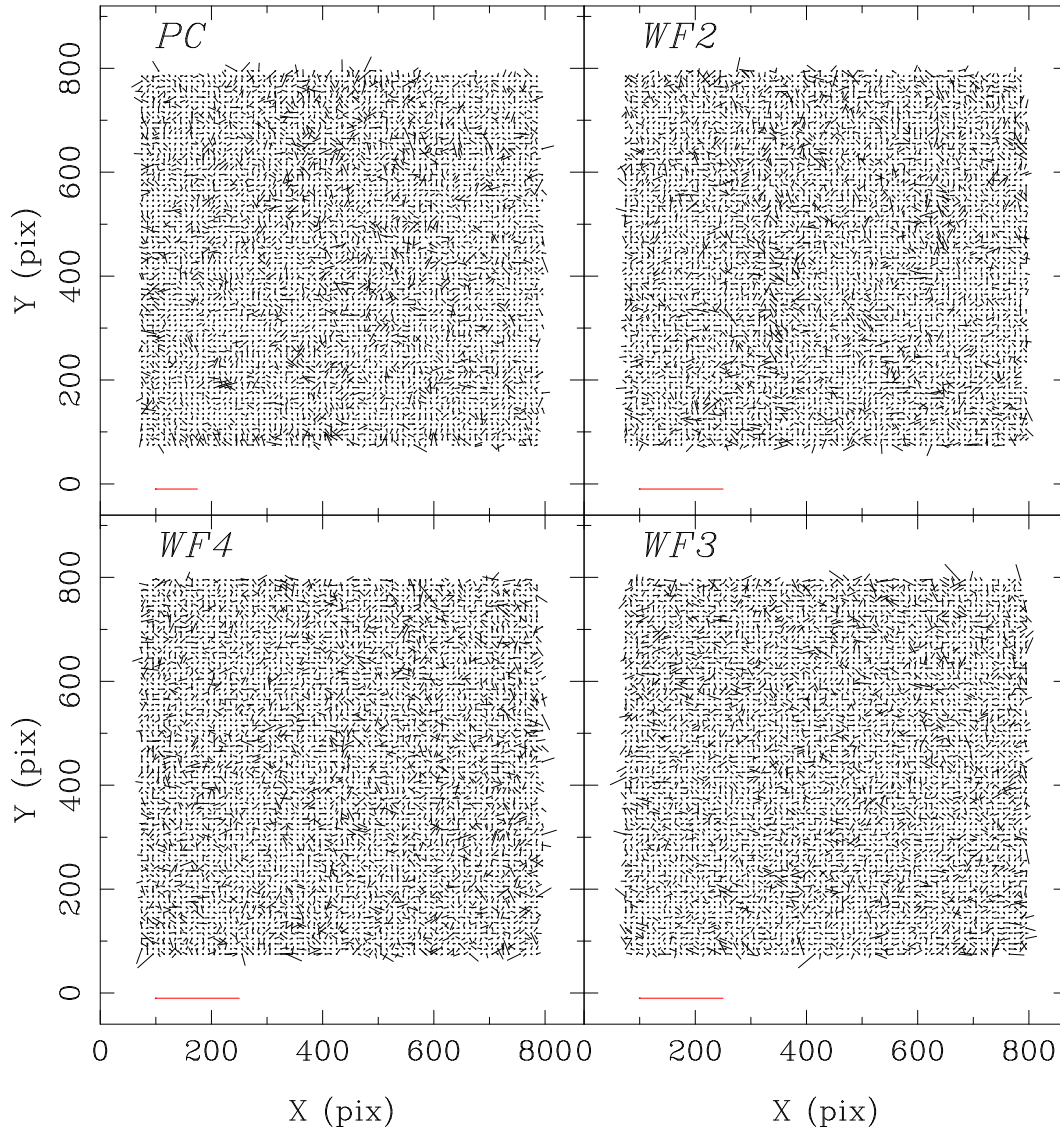


Figure 4. Map of residuals with 10-pixel resolution element. Any resolution element that had an average residual $|r| > 20$ mpix for the PC and $|r| > 10$ mpix for the WF was excluded from the map, thus eliminating some outlier resolution elements. At the edges, resolution elements with large residuals still can be found. However, no regular, distinct pattern can be discerned from this map. The horizontal line in the bottom left of each panel represents a vector of 50 mpix size.

Table 4. Median error (in mpix) per resolution element in the x-coordinate for the 50-pix resolution map

	2DG			ePSF		
	error	N/cell	N_{all}	error	N/cell	N_{all}
<i>Gaia</i> EDR3						
<i>F555W</i>						
PC	9.6	2169	143120	11.2	1730	113367
WF2	2.0	6416	441392	2.4	3851	271620
WF3	2.0	6169	416067	2.5	3631	254464
WF4	1.9	6534	440822	2.2	4030	279304
<i>F606W</i>						
PC	9.5	961	63347	15.0	529	54188
WF2	1.7	4976	323628	3.1	1563	290753
WF3	1.7	4474	323285	3.2	1610	290193
WF4	1.6	5058	328403	2.9	1725	295793
<i>F814W</i>						
PC	10.2	1771	116730	12.1	1405	93192
WF2	1.8	6156	405651	2.3	3470	345662
WF3	1.9	5991	394326	2.4	3696	340264
WF4	1.8	6281	414623	2.3	3895	354668
47 Tuc - off center						
<i>F555W</i>						
PC	6.2	115	9611	5.4	108	9197
WF2	2.9	480	34386	1.8	474	33119
WF3	4.2	265	18463	3.2	235	17518
WF4	4.3	261	18520	3.1	262	18851
<i>F606W</i>						
PC	2.6	325	22743	2.0	305	21090
WF2	1.7	1310	86418	0.9	1195	80089
WF3	1.6	1280	84536	1.0	1199	80000
WF4	1.8	1249	83027	0.9	1174	78510
<i>F814W</i>						
PC	3.8	129	9038	3.5	125	8844
WF2	2.2	682	46208	1.5	646	44053
WF3	2.5	558	37329	1.9	527	36074
WF4	2.8	456	31489	1.9	444	30771
ω Cen - center						
<i>F555W</i>						
PC	6.2	269	17957	4.0	266	17761
WF2	5.1	363	26334	2.8	453	32766
WF3	4.8	473	30961	2.9	555	37262
WF4	4.1	588	39840	2.3	726	49725

into-ePSF map adds negligibly to the target-map uncertainties.

From this point on, all 2DG-based maps are adjusted to the ePSF-centering system upon their construction. To emphasize their modified nature, we will refer to such maps (and cubic terms) as 2DG*.

In addition to the high-order field effects induced by the different centering schemes, we point out that the cubic terms are also affected. As such, we calculate the mean cubic terms in the 2DG-into-ePSF solutions and use these as adjustments to any standard-catalog derived 2DG-based cubic terms. The resulting 2DG* cubic terms are then applicable to ePSF-determined positions.

We have chosen to work in the system of ePSF centering because it is, without doubt, the more common standard of the two for astrometric processing of WFPC2 images.

7.2.3. Remaining Map Differences

Differences between maps derived from standard catalogs are examined to determine if they are significant, with respect to the uncertainties of the standard catalogs and the centering precision of the WFPC2 images. For each resolution element we calculate a difference divided by its estimated formal error. If the difference in maps is merely random, the normalized differences should distribute around zero with a standard deviation of 1. We determine the standard deviation of the normalized differences σ_s using probability plots (Hamaker 1978) with trimming of the extreme 10% of both wings to alleviate the effect of possible outliers.¹ To demonstrate, we apply the procedure to maps based on the same standard catalog, centering algorithm, and filter and consider differences between chip WF2 and the other three chips. The calculated map-difference dispersions have values around 2.0. The smoothing used during the construction of these low-frequency maps effectively decreases the number of independent resolution elements by a factor of π , from 15×15 to ~ 72 . Thus, the uncertainty in a dispersion measure of 2.0 will be ~ 0.2 , indicating that indeed the map of WF2 is significantly different from the maps of the other three chips.

Figure 5 shows this statistic (σ_s) for differences between maps based on the 2DG* and the ePSF algorithms, i.e., after having adjusted the 2DG maps as described in Sec. 7.2.2. For filters F555W and F814W the dispersion of the normalized differences σ_s has values close to 1, indicating that differences in centering algorithms are not discernable in these maps. For filter F606W, σ_s has values closer to 1.5 for the wide-field chips, hinting at some remaining difference between centering algorithms. This is possibly related to the use of

¹ The probability-plot method is a robust estimator of mean and standard deviation of a supposed Gaussian distribution of values. Comparing the value-ordered spacing of the central portion of the set of values with that expected for a similarly sized Gaussian sample renders it less susceptible to spurious outlier points in the wings.

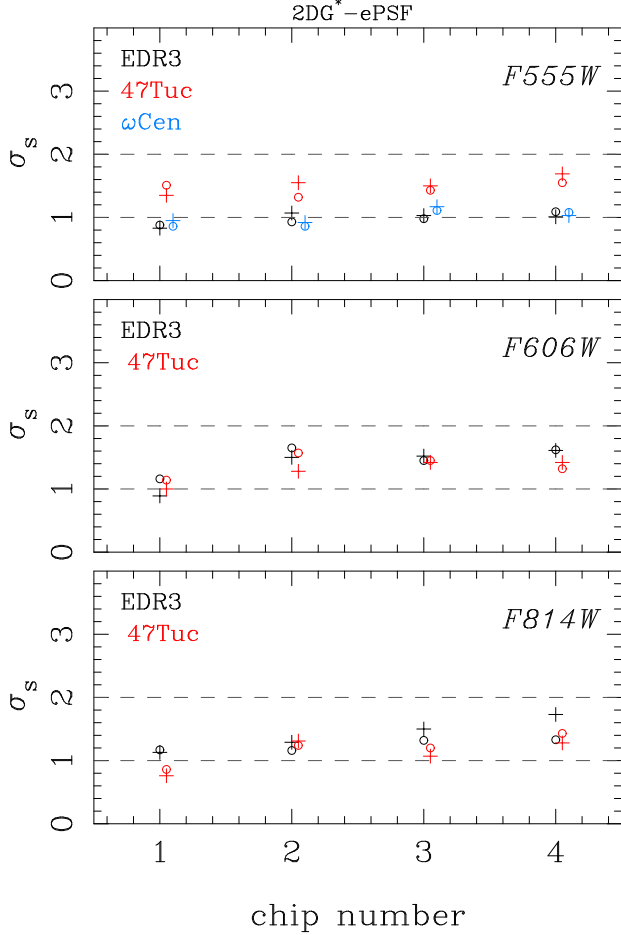


Figure 5. Dispersions of the error-normalized differences comparing maps derived from standard catalogs, based on 2DG* and ePSF centers. Color-coding, as labeled, indicates the standard catalog used in constructing the maps being compared. Each panel presents results for a different filter. The dispersion statistic for differences between x-coordinate maps are plotted with circles, results for y-coordinate maps are represented with plus signs.

the F555W effective-psf library for the ePSF centering of the F606W images, the best available option at this time. Our overall conclusion is that centering algorithm differences are not appreciably affecting the distortion maps, provided the 2DG-center maps are properly adjusted. This will allow us to average maps based on the two different centering schemes.

In Figure 6 we show σ_s for map differences between filters. Values of $\sigma_s \sim 2$ are obtained for differences between F555W and F606W indicating that the distortion maps are different for these filters. The difference between F555W and F814W is less striking with $\sigma_s \sim 1.5$. In general, filter differences do appear significant and thus we will provide separate maps for each filter.

8. ADOPTED DISTORTION MODEL

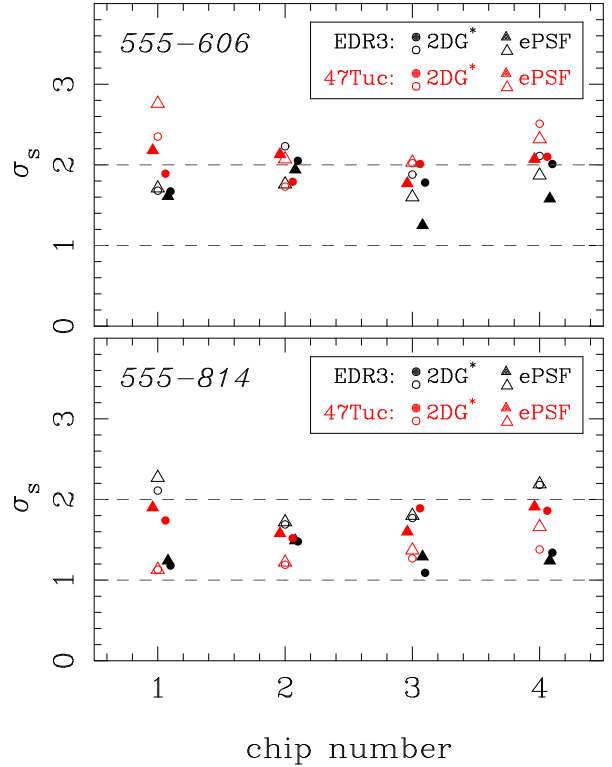


Figure 6. Dispersions of the error-normalized differences comparing maps derived in different filters. The top panel shows statistics for map differences between F555W and F606W; the bottom panel compares F555W and F814W maps. Comparisons of EDR3-based maps are shown with black symbols, while the 47Tuc-based map differences are shown in red. Differences for 2DG*-algorithm maps are represented with circles, while the ePSF maps are represented with triangles. Filled symbols depict x-coordinate map results, open symbols depict y-coordinate results.

Corrections to the nominal distortion model that we present consist of a) third-order terms based on EDR3 solutions of 2DG* positions, i.e., the terms are adjusted to be applicable to ePSF-determined positions. and b) higher than third order residual maps based on a combination of EDR3, 47 Tuc and ω Cen standard catalogs. The coefficients of the third order terms are given at two average epochs: an early epoch (< 2005.0) and a late epoch (≥ 2005.0). EDR3 solutions by far outnumber solutions from the other standard catalogs (see Tab. 2). Therefore we determine each coefficient by averaging solely the EDR3 solutions for each chip, filter and epoch group. In Table 5 we list these coefficients together with the average epoch. When calculating the correction for a given observation we choose to use a linear interpolation/extrapolation between these two mean epochs to determine the applicable cubic coefficients. Alternatively, the user can decide in which epoch group the observation is, and directly use the coefficients listed

in Tab. 5. Variations with time are mild, nevertheless significant in some cases (see Tab. 5).

Higher than third-order distortion residual maps are built at a resolution of 50 pixel and at single epoch. We have explored time variations in the distortion maps. Unfortunately, for the late epoch (> 2005) there are few WFPC2 observations compared to earlier data, and thus late-epoch maps are rather noisy due to the scarcity of residuals. To this end, we could not convincingly find a time dependence of these maps.

For the final maps we combine residuals from the following solutions: EDR3 with 2DG* positions, 47 Tuc with ePSF positions and ω Cen with ePSF positions. According to Tab. 4, these solutions have the best median error per resolution element. We adopt a weighted mean, where the weight is determined from the estimated uncertainty of each resolution element which in turn was based on the scatter and number of residuals per element. Maps are constructed for each chip and filter; these are presented in Figures 7, 8 and 9. Higher-order systematics are readily apparent in the maps. The $\langle \chi^2 \rangle$ (see eq. 2) for these maps ranges between 7 and 70.

The corrections derived here represent small post-corrections to the nominal third-order distortion determined by AK03. For instance, the nominal AK03 cubic-distortion corrections exhibit an amplitude of up to 4 pixels from chip center to edge (both PC and WF). Inspection of the newly determined (post-nominal correction) cubic terms in Tab. 5, shows that the largest terms are $\sim 300 \times 10^{-11}$ pix/pix³ for the PC, and $\sim 100 \times 10^{-11}$ pix/pix³ for the WF. These corrections are on the order of 0.1 pixels, chip center to edge.

To better compare the relative size of these corrections, we generate 10,000 randomly located points over the chip and calculate at each location the size of the distortion as given by AK03, by our third-order correction, and by higher than third order corrections. Epoch is also randomly assigned for the purpose of calculating our third-order corrections. We calculate the rms values, $\sqrt{(dx^2 + dy^2)}$, where dx and dy are the correction values in each axis. We tabulate these rms values for each chip and filter in Table 6. Our third-order correction is at a level of a few percent that from AK03 for the PC, and around 1% for the WF. The higher-order corrections are between $\sim 18\%$ and 90% the size of our cubic-term correction.

The third order coefficients from Tab. 5, the higher-order distortion maps and a Fortran subroutine to apply these corrections are included as a digital archive accompanying this manuscript.

9. SUMMARY AND FUTURE WORK

We explore systematic distortions in WFPC2 exposures, in filters F555W, F606W and F814W. These are beyond the previously determined 34th-row correction and nominal cubic distortion characterized by AK99 and AK03. Our study examines high- and low-frequency spatial systematics by stacking hundreds of thousands of residuals from transformations into three standard catalogs, and from relative transformations between WFPC2 exposures. In the high-frequency domain, to a resolution of 10 pixels, we find no other systematics beyond the well-known 34th-row correction. In the low-frequency domain, on scales of 50 pix and larger, we find significant systematics beyond the nominal AK03 distortion. We characterize these systematics with third-order coefficients and distortion maps presented for each filter and chip. *Gaia* EDR3 is crucial to this calibration, being the one catalog that allows for such an extensive mapping of the geometric distortions in WFPC2.

The modifications to the nominal (AK03) WFPC2 distortion corrections we present range in size from less than 10 mpix up to ~ 50 mpix. For an individual star, random measuring errors typically will be or order 20 mpix. The effects of CTE and exposure-to-exposure variation of distortions across a chip can be expected to be of this size or more. For this reason, the corrections we present are of most value in statistical studies involving many stars and multiple exposures.

As part of the distortion exploration, we perform a comparative analysis of five centering algorithms for WFPC2 star images. This allowed us to better understand how each algorithm performs, and to select the most appropriate algorithm for our purpose. A direct comparison of 2DG-derived positions with those from the ePSF algorithm demonstrated spatial variations between the two that must be accounted for. The modifications to the nominal AK03 distortion corrections we present are applicable to ePSF-derived positions.

An interesting finding of our centering-algorithm tests is that PSFEX is a promising astrometric choice, or at the least one that can be used in some specific targeted astrometric studies, given its computational needs. An issue that remains to be better studied is that of the pixel-phase bias, which operates across the scale of a pixel. It is a consequence of detector undersampling and the unavoidable uncertainty in the assumed profile of stellar images, and is most critical for the WF chips. Although the ePSF algorithm performs well in this regard, the pixel-phase effect is still present at some level. Correction for the effect should be improved upon, if highest astrometric precision is to be achieved. This will be the topic of a future study. The maps built and

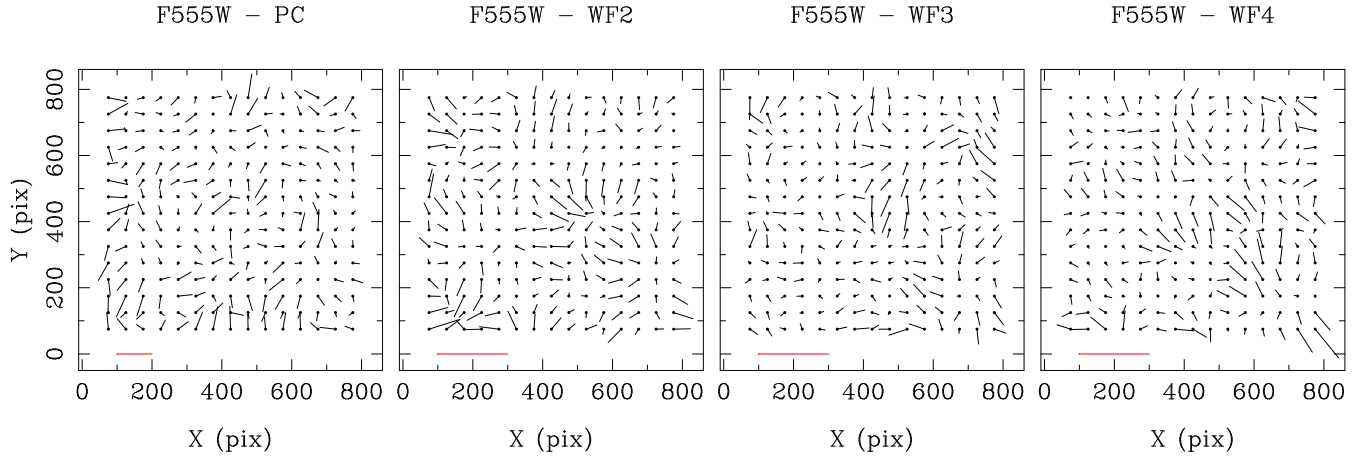


Figure 7. Distortion-correction maps, post third-order correction. All maps have a resolution of 50 pixels, and are constructed from a weighted average of EDR3, 47 Tuc and ω Cen standard catalogs (see text). Here we show maps for filter F555W. The origin of each vector is marked with a black dot. The horizontal line at the bottom left of each plot represents a vector of 10 mpix size.

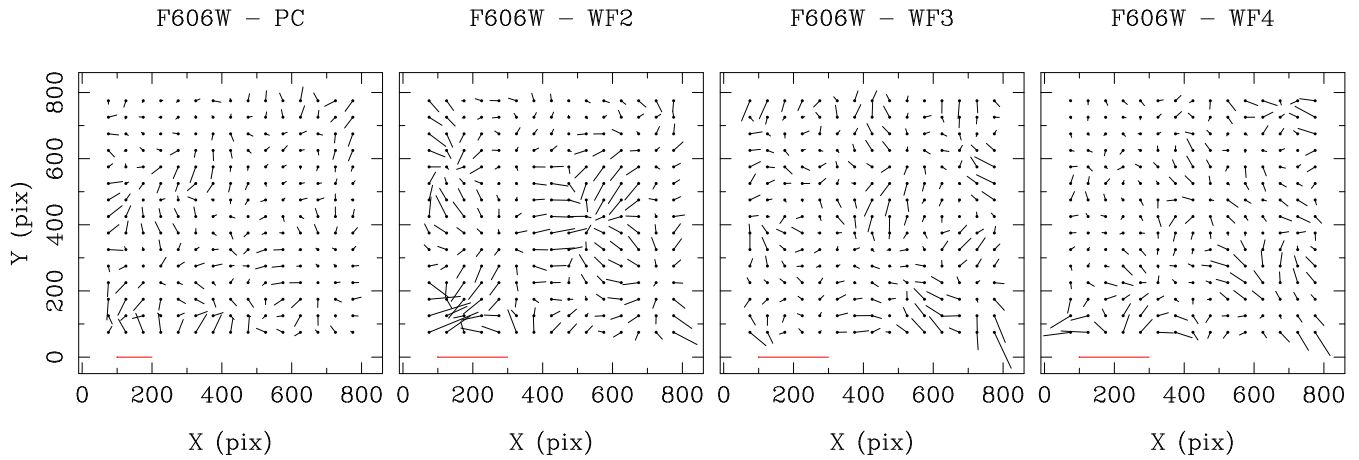


Figure 8. Same as in Fig. 7 only for filter F606W. Again, the horizontal line at the bottom left of each plot represents a vector of 50 mpix size.

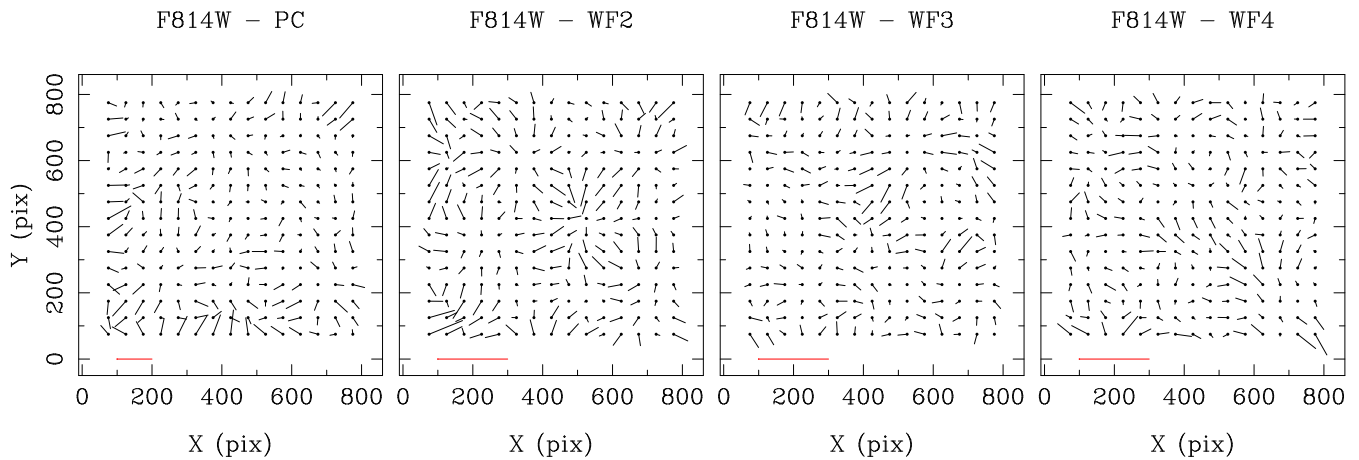


Figure 9. Same as in Fig. 7 only for filter F814W. The horizontal line at the bottom left of each plot represents a vector of 50 mpix size.

Table 5. Average cubic terms of the EDR3 2DG* solutions, (on the ePSF system). Units are 10^{-11} pix/pix³

<i>< epoch ></i>	XXX	XXY	XYX	YYY	YYY	YYX	YXX	XXX
	<i>F555W — X-sol.</i>				<i>F555W — Y-sol.</i>			
PC								
1997.76	-039(028)	078(027)	-158(025)	-019(029)	-009(027)	-050(027)	-136(026)	008(024)
2008.05	-135(025)	136(028)	-096(023)	-098(026)	-182(022)	070(024)	103(025)	176(023)
WF2								
1998.15	013(006)	-049(005)	-013(005)	-043(005)	-011(006)	010(005)	-038(006)	-011(006)
2007.70	-006(006)	-034(006)	-014(006)	-069(007)	-002(007)	012(007)	-037(007)	008(007)
WF3								
1998.13	-001(006)	019(005)	019(006)	-031(006)	-005(006)	028(006)	007(006)	-004(006)
2007.66	018(006)	005(006)	010(005)	-029(005)	-011(006)	-014(005)	041(006)	002(007)
WF4								
1998.15	005(006)	-015(005)	-022(005)	-039(005)	026(006)	-051(006)	-007(005)	005(006)
2007.71	-013(006)	-009(006)	-018(006)	-074(006)	-025(007)	-025(006)	003(006)	036(007)
	<i>F606W — X-sol.</i>				<i>F606W — Y-sol.</i>			
PC								
2000.88	-079(027)	-021(027)	-064(028)	158(029)	-097(028)	-168(034)	081(028)	102(026)
2007.08	-317(055)	-196(047)	026(044)	-052(038)	-076(039)	-005(032)	066(030)	-061(038)
WF2								
2000.97	047(005)	-006(005)	-015(005)	-006(005)	-017(006)	021(005)	009(005)	-008(005)
2007.77	-007(010)	-009(009)	-045(009)	007(008)	-056(011)	021(009)	-038(011)	-002(009)
WF3								
2000.96	005(005)	017(005)	019(005)	-028(005)	040(006)	003(005)	-036(006)	037(005)
2007.64	-021(008)	066(008)	013(008)	-056(008)	042(009)	-008(010)	-042(008)	017(008)
WF4								
2000.95	013(005)	-030(005)	-013(005)	-032(004)	024(005)	-069(005)	-006(006)	-012(006)
2007.65	026(009)	-064(008)	-024(007)	-017(008)	016(008)	-055(007)	-006(010)	-021(009)
	<i>F814W — X-sol.</i>				<i>F814W — Y-sol.</i>			
PC								
1998.39	002(021)	014(023)	-116(022)	102(024)	-025(024)	-094(023)	-016(022)	029(020)
2007.12	-112(033)	-100(030)	-097(029)	-038(026)	022(026)	004(026)	125(027)	024(026)
WF2								
1998.69	050(004)	-077(004)	038(005)	-014(004)	006(005)	-022(005)	070(005)	-024(005)
2007.16	028(006)	-066(006)	023(005)	-021(007)	-007(006)	-003(005)	042(007)	001(007)
WF3								
1998.63	033(005)	008(004)	045(005)	-025(005)	016(005)	002(004)	053(005)	015(005)
2007.11	021(006)	022(006)	057(005)	-035(006)	045(007)	-027(005)	021(006)	001(007)
WF4								
1998.62	003(004)	-063(004)	063(004)	-020(004)	046(005)	-102(004)	075(004)	-007(005)
2007.12	034(006)	-066(005)	060(006)	-014(005)	038(007)	-085(006)	130(007)	-007(006)

Table 6. RMS values of various distortion corrections, and their ratios. Correction types are: $\delta 1$ for AK03, $\delta 2$ for our third-order corrections, and $\delta 3$ for the higher-order distortion maps.

Filter	$\delta 1$	$\delta 2$	$\delta 3$	$\delta 2/\delta 1$	$\delta 3/\delta 1$	$\delta 3/\delta 2$
:chip	(mpix)	(mpix)	(mpix)	(%)	(%)	(%)
555:1	1580.2	46.0	14.1	2.9	0.9	30.6
606:1	1589.0	66.7	11.7	4.2	0.7	17.5
814:1	1590.8	35.3	12.7	2.2	0.8	35.8
555:2	1470.4	16.5	7.4	1.1	0.5	44.8
606:2	1467.9	14.6	9.4	1.0	0.6	63.8
814:2	1468.0	19.8	7.4	1.3	0.5	37.5
555:3	1486.4	6.9	6.3	0.5	0.4	90.1
606:3	1493.7	12.0	6.8	0.8	0.5	57.0
814:3	1525.2	16.3	5.5	1.1	0.4	33.3
555:4	1488.6	14.2	6.9	1.0	0.5	48.2
606:4	1493.2	15.6	6.4	1.0	0.4	40.9
814:4	1507.0	28.9	5.8	1.9	0.4	20.2

presented in the current study, however, are not affected by this effect as its contribution is effectively as random noise participating at a level well below that of other sources of random error.

Finally, an important aspect that remains to be explored in a future study is that of charge transfer efficiency, CTE, which can have considerable astrometric impact, especially for short exposures with WFPC2.

While the size of CTE-induced offsets can be considerable, their effect on the purely geometric corrections presented here is to add a negligible amount of uncertainty due to marginalizing over stellar magnitude. Our hope is to employ *Gaia* EDR3 in the future to derive an empirically based procedure for CTE correction of WFPC2.

This work was supported by grant HST-AR-15632 from the Space Telescope Science Institute, STScI, operated by AURA. We wish to thank the MAST personnel for providing the entire WFPC2 data set to us on physical media; ours was an unusual request that was not feasible using the online query tool and the MAST personnel accommodated us graciously.

This study has made use of data from the European Space Agency (ESA) mission *Gaia* (<https://www.cosmos.esa.int/gaia>) processed by the Gaia Data Processing and Analysis Consortium (DPAC, <https://www.cosmos.esa.int/web/gaia/dpac/consortium>). Funding for the DPAC has been provided by national institutions, in particular the institutions participating in the *Gaia* Multilateral Agreement.

We are grateful to an anonymous referee whose suggestions helped us greatly improve this manuscript over an earlier version.

Facilities: HST (WFPC2), MAST, *Gaia*

REFERENCES

- Anderson, J. & King, I. R. 1999, *PASP*, 111, 1095
- Anderson, J. & King, I. R. 2000, *PASP*, 112, 1360
- Anderson, J. & King, I. R. 2003, *PASP*, 115, 113
- Bellini, A., Bianchini, P. Varri, A. L., Anderson, J., Piotto, G., van der Marel, R. P., Vesperini, E & Watkins, L. 2017, *ApJ*, 844, 167
- Bertin, E. & Arnouts, S. 1996, *A&AS*, 117, 393
- Bertin, E. & Arnouts, S. 2010, 2010ascl.soft10064B
- Benedict, F. 2017, *PASP*, 129, 2001
- Dolphin, A. E. 2000, *PASP*, 112, 1383
- Dolphin, A. E. 2009, *PASP*, 121, 655
- Gaia* Collaboration, Brown, A. G. A., Vallenari A., et al. 2016, *A&A*, 595, A2
- Gaia* Collaboration, Brown, A. G. A., Vallenari A., et al. 2018a, *A&A*, 616, A1
- Gaia* Collaboration, Helmi, A., van Leeuwen, F., et al. 2018b, *A&A*, 616, A12
- Gaia* Collaboration, Lindegren, L., Hernandez, J., et al. 2018b, *A&A*, 616, A2
- Gaia* Collaboration, Evans, D. W., Riello, M. et al. 2018c, *A&A*, 616, A4
- Gaia* Collaboration, Babusiaux, C. van Leeuwen, F. et al. 2018d, *A&A*, 616, A10
- Gaia* Collaboration, Brown, A. G. A., Vallenari, A. et al. 2020, *A&A*, in press, arXiv:2012.01533
- Hamaker, H. C. 1978, *Applied Statistics*, 27, 7
- Kallivayalil, N., van der Marel, R. P., Anderson, J., Besla, G., & Alcock, C. 2013, *ApJ*, 764, 161
- Kozhurina-Platais, V., Anderson, J. & Koekemoer, A. M. 2003, Instrument Science Report WFPC2 2003-02 (Baltimore, MD:STScI)
- Kozhurina-Platais, V. & Anderson, J. 2015, Instrument Science Report WFC 2015-02 (Baltimore, MD:STScI)
- Kozhurina-Platais, V., Borncamp, D., Anderson, J., Grogin, N., & Hack, W. 2015, Instrument Science Report ACS 2015-06 (Baltimore, MD:STScI)
- Kozhurina-Platais, V., MacKenty, J. Golimovski, D., Sirianni, M., Borncamp, D., Anderson, J. & Grogin, N. 2016, *SPIE* 9904, 6I

- Kozhurina-Platais, V., Grogan, N. & Sabbi, E. 2018, Instrument Science Report ACS 2018-01 (Baltimore, MD:STScI)
- Krist, J. E., Hook, R. N., & Stoehr, F. 2011, SPIE, 8127, id. 81270J
- Lee, J.-F., & van Altena, W. F. 1983, AJ, 88, 1683
- Massari, D., Fiorentino, G., McConnachie, A., Bellini, A., Tolstoy, E., Turri, P., Andersen, D., Bono, G., Stetson, P. B., & Veran, J.-P. 2016, A&A, 595, L2
- Patti, M & Fiorentino, G. 2019, MNRAS, 485, 3470
- Riess, A. G., Macri, L. M., Hoffmann, S. L., Scolnic, D., Casertano, S., Filippenko, A. V., Tucker, B., E., Reid, M., J., Jones, D. O., Silverman, J. M., Chornock, R., Cahllis, P., Yuan, W., Brown, P. J., & Foley, R. J. 2016, ApJ, 826, 56
- Sohn, S. T., Watkins, L. L., Fardal, M. A., van der Marel, R. P., Deason, A. J., Besla, G., & Bellini, A. 2018, ApJ, 862, 52
- Woodley, K. A. 2012, ApJ751, L12
- Sohn, S. T., Patel, E. Besla, G., van der Marel, R. P., Bullock, J. S., Strigari, L. E., van de Ven, G., Walker, M. G., & Bellini, A. 2017, ApJ, 849, 93
- Watkins, L. L., van der Marel, R. P., Bellini, A. & Anderson, J. 2015, ApJ, 803, 29